# Dependence of the turbulent particle flux on hydrogen isotopes induced by collisionality

C. Angioni[1], E. Fable[1], P. Manas[1], P. Mantica[2], P. A. Schneider[1], the ASDEX Upgrade Team, the EUROfusion MST1 Team[3] and JET contributors[4]

[1] *Max-Planck-Institut für Plasmaphysik, 85748 Garching bei München, Germany*

[2] *Istituto di Fisica del Plasma, CNR/ENEA, Milano, Italy*

[3] *See the author list of "H. Meyer et al 2017 Nucl. Fusion 57 102014"*

[4] *See the author list of "X. Litaudon et al 2017 Nucl. Fusion 57 102001"*

(Dated: August 8, 2018)

## Abstract

The impact of the change of the mass of hydrogen isotopes on the turbulent particle flux is studied. The trapped electron component of the turbulent particle convection induced by collisionality, which is outward in ion temperature gradient turbulence, increases with decreasing thermal velocity of the isotope. Thereby, the lighter is the isotope, the stronger is the turbulent pinch, and the larger is the predicted density gradient at the null of the particle flux. The passing particle component of the flux increases with decreasing mass of the isotope, and can also affect the predicted density gradient. This effect is however subdominant for usual core plasma parameters. The analytical results are confirmed by means of both quasi–linear and nonlinear gyrokinetic simulations, and an estimate of the difference in local density gradient produced by this effect as a function of collisionality has been obtained for typical plasma parameters at mid–radius. Analysis of currently available experimental data from the JET and the ASDEX Upgrade tokamaks **does not show any clear and general evidence of inconsistency with this theoretically predicted effect outside the errorbars, and also allows the identification of some cases of qualitative consistency**.

PACS numbers: 52.25.Fi, 52.35.Ra, 52.55.Fa

## I. INTRODUCTION

The understanding of the differences in the properties of transport and confinement of tokamak plasmas when changing the main ion species is a critical component towards the capability of predicting of fusion reactor plasma, where a mixture of deuterium D and tritium T will be used. Many studies have been dedicated to the comparison of the global confinement properties when changing the hydrogen (H) isotope as main ion species [1–16], with increasing emphasis recently also dedicated to the understanding of changes in the transport properties more than just in the global confinement, also from a theoretical perspective [17–20]. The observation that the confinement increases with increasing mass of the H isotope is in contraddiction with simple expectations based on an overall gyro-Bohm scaling of local transport, but allows more optimistic expectations when considering the D–T fuel mixture as compared to present experiments which are predominantly performed in D. The recent and the forthcoming campaigns at JET with different H isotopes, including T, have strongly renewed the interest in achieving a deeper understanding of the physics of transport and confinement related to a change of the H isotope as main ion. While a large part of these studies are dedicated to the global confinement properties and to the heat transport, less emphasis has been given to the understanding of the potential differences in particle transport, which also can play a critical role if differences between the density profiles of the two fuel reactants are present. A previous gyro–kinetic study dedicated to a mixture of D and T in equal fractions identified a small particle flux asymmetry between T and D, present even in the adiabatic electron limit, with T flowing inward and D flowing outward [21]

In this paper, we consider the problem from a theoretical persepective and we focus on plasmas with a single ion species given by a H isotope, that is, H, D or T. We point out the existence of a turbulent transport mechanism, connected with the effect of electron–ion collisions on the radial flux of trapped electrons, by which the turbulent convection with different H isotopes is predicted to be different, leading to stronger inward convection with decreasing mass of the isotope. A simple analytical model is introduced to clarify the main physical ingredients at play in Section 2. In Section 3, a set of numerical simulations with the gyrokinetic code GKW [22] are performed in order to better illustrate the dependences and to more precisely quantify the magnitude of the effect. This collisionality induced effect

is predicted to be the dominant one at typical core plasma parameters. Other mechanisms of particle transport, particularly connected with parallel electron dynamics, are shown to produce smaller effects as a consequence of a change of the ion mass. In Section 4, recent experimental data from ASDEX Upgrade (AUG) and JET are examined in order to investigate whether the predicted effect is at least qualitatitvely consistent with the observations. Finally section 5 draws the conclusions of this work.

## II. ANALYTIC MODEL

In the limit of adiabatic electrons, the gyrokinetic equation of the ions can be normalized in a form which is invariant to a change of the mass of the ions [17]. The inclusion of kinetic electrons introduces terms, in particular connected with the parallel dynamics, the electromagnetic effects and the electron–ion collisions, which directly depend on the electron to ion mass ratio and thereby break this invariance. In the present analytical model, we follow the derivation presented in Ref. [23]. We consider the linearized electrostatic version of the gyrokinetic equation where the effect of the collisions is included by means of a simple **energy–independent** Krook operator. The non–adiabatic part $g_k$ of the perturbed electron distribution function $f_k = g_k + F_M J_0 \hat{\phi}$, for a single toroidal mode number $n = k_y r/q$, with $k_y$ the binormal wave number, $r$ the local minor radius of the plasma, and $q$ the local safety factor, is decomposed in Fourier harmonics $g_k = \hat{g}_k \exp(-i\omega t + i\mathbf{k}\cdot\mathbf{X})$. **We recall that the distribution fuctions are defined on the gyrocenter coordinates X while the electrostatic potential $\phi$ is defined on the particle coordinates x. In the spectral representation applied here, the gyro-averaging introduces the Bessel function factor $J_0$, with the electrostatic potential function of the gyrocenter coordinates. We also note that the main physical results of this derivation can be also obtained in the framework of a drift-kinetic description.** In the simple $s-\alpha$ circular shifted geometry described by a limited set of local parameters, the inverse aspect ratio $\epsilon = r/R$, the safety factor $q$, the magnetic shear $s = r\,dq/dr\,/q$, and $\alpha = -q^2 R\, 2\mu_0\, dp/dr\,/B^2$, with $p$ the total plasma pressure, the gyrokinetic equation reads,

$$(\omega - \omega_{Gk} + i\nu_{ei})\ \hat{g}_k = \left\{ \omega_{Dk} \left[ \frac{R}{L_n} + \left( \frac{E}{T_e} - \frac{3}{2} \right) \frac{R}{L_{Te}} \right] - \omega \right\} F_M J_0(k_\perp \rho_s)\, \hat{\phi}_k. \tag{1}$$

The Krook collision operator describes electron–ion collisions, with a collision frequency $\nu_{ei} = (Z_i^2 e^4 \ln\Lambda_{ei} n_i)/(4\pi\epsilon_0^2 m_e^{1/2} T_e^{3/2})$. **We notice that an energy dependent factor in the collision frequency can also be introduced in this analytical description, as in Ref. [24], in order to also describe the stronger effect of collisions on slow particles. However, this element is not included here since it does not play a critical role in the identification of the differences among hydrogen isotopes**. On the left hand side, the motion of the gyrocenters is described by the total frequency $\omega_{Gk} = k_\parallel v_\parallel + \omega_{dk}$, where the derivative along the field line has been formally replaced by a parallel wave number $k_\parallel$. The perpendicular drift frequency arising from the $\nabla B$ and curvature drifts is $\omega_{dk} = \omega_{Dk}[(v_\parallel^2 + v_\perp^2/2)/v_{the}^2][\cos\theta + (s\theta - \alpha\sin\theta)\sin\theta]$, with $\theta$ the extended ballooning angle and with the fluid drift frequency $\omega_{Dk} = k_y T_e/eBR = k_y \rho_{si} c_{si}/R$. The Larmor radius $\rho_{si} = c_{si}/\Omega_{ci}$ is defined with the sound speed $c_{si} = \sqrt{T_e/m_i}$, with $\Omega_{ci}$ the ion cyclotron frequency. At the right hand side, the normalized logarithmic gradients of the equilibrium density and temperature $R/L_n = -Rdn/dr/n$ and $R/L_{Te} = -RdT_e/dr/T_e$ stem from the radial derivative of the equilibrium Maxwellian distribution $F_M$. $R$ is the major radius at the center of the magnetic flux surface, $E$ the kinetic energy of the particle. Finally, the fluctuating electrostatic potential has been normalized as usual $\hat{\phi}_k = e\phi_k/T_e$.

We normalize all frequencies to the fluid perpendicular drift frequency $\omega_{Dk} = k_y T_e/eBR$, to obtain,

$$(\hat{\omega}_k - \hat{\omega}_{Gk} + i\hat{\nu}_{ei})\ \hat{g}_k = \left\{ \left[ \frac{R}{L_n} + \left( \frac{E}{T_e} - \frac{3}{2} \right) \frac{R}{L_{Te}} \right] - \hat{\omega}_k \right\} F_M J_0(k_\perp \rho_s)\, \hat{\phi}_k. \tag{2}$$

The quasi–linear particle flux $\Gamma_{QL}$ produced by the fluctuating $E \times B$ drift $\tilde{v}_{E\times B}$ is $\langle \tilde{n}_e \tilde{v}_{E\times B} \rangle$, where the brackets express flux surface average.

By formally computing the linear phase shift between density and electrostatic potential fluctuations from Eq. (2), we obtain the following expression for the particle flux, where, following [23], separate integrations in velocity space are performed for trapped and passing electrons, assuming **deeply trapped electrons** and a **nearly**–adiabatic passing electron response. **For the nearly–adiabatic passing electrons, the streaming term $k_\parallel v_\parallel$ at the left hand side of the gyrokinetic equation is considered to be dominant, and the expansion on the small parameters $\gamma/(k_\parallel v_\parallel) << 1$ and $\omega_r/(k_\parallel v_\parallel) << 1$ allows the analytical calculation of the kinetic integral by applying the Sokhotski-Plemelj**

**theorem.**

$$\Gamma_{n\,QL} = f_t\,\Gamma_{nt} \;+\; (1-f_t)\,\Gamma_{np}, \tag{3}$$

where

$$\Gamma_{n\,t} = c_s\sqrt{\frac{2}{\pi}}\sum_k k_y\rho_s\left\langle|\hat{\phi}_k|^2\int\sqrt{E}\,dE\,J_0(k_\perp\rho_b\sqrt{2E/T_e})^2\cdot\right.$$
$$\left.\cdot\,\frac{(\hat{\gamma}_k+\hat{\nu}_k)[R/L_n+(E/T_e-3/2)R/L_{Te}]-(\hat{\gamma}_k\hat{\omega}_{dk}-\hat{\omega}_{rk}\hat{\nu}_k)}{(\hat{\omega}_{rk}+\hat{\omega}_{dk})^2+(\hat{\gamma}_k+\hat{\nu}_k)^2}\right\rangle \tag{4}$$

and

$$\Gamma_{n\,p} = c_s\sqrt{\frac{\pi}{2}}\sum_k k_y\rho_s\left\langle|\hat{\phi}_k|^2\right\rangle\;\frac{k_y\rho_s\,c_s}{R|k_\parallel v_{the}|}\left(\frac{R}{L_n}-\frac{1}{2}\frac{R}{L_{Te}}+\hat{\omega}_{rk}\right) \tag{5}$$

where $\gamma_k$ and $\omega_{rk}$ are the growth rate and real frequency of the unstable linear mode. We recall that all frequencies have been normalized to the fluid perpendicular drift frequency $\omega_{Dk} = k_y T_e/eBR = k_y\rho_{sp}c_{sp}/R$, where we introduce the proton mass $m_p$ in expressing the normalizing drift frequency in terms of the normalized binormal wave number $k_y\rho_{sp}$ and the sound speed $c_{sp}$, with $c_{sp} = (T_e/m_p)^{0.5}$ and $\rho_{sp} = c_{sp}/\Omega_{cp}$, regardless the mass of the ion species, that is of the H isotope. The sign convention is that a positive value of the real frequency $\hat{\omega}_{rk}$ identifies a mode propagating in the ion diamagnetic direction, that is, an ion temperature gradient (ITG) mode. The quasi–linear flux is computed by considering the complex linear eigenfrequency $\omega_{rk}+i\gamma_k$, where the growth rate describes the turbulent spectral broadening, as is customary in transport models. **In the expression for the flux of deeply trapped electrons Eq. (4), the banana width $\rho_b$ appears in the argument of the Bessel function $J_0$, after having performed the bounce average.**

We specifically consider the collisional convective contribution to the particle flux which is produced by trapped electrons, Eq. 4 (and also derived in Eq. 16 of [23]). We observe that, in the case of ITG turbulence, that is with positive $\hat{\omega}_{rk}$, this produces at each wave number $k_y$ an outward contribution to the particle flux proportional to

$$\hat{\omega}_{rk}\,\hat{\nu}_k = \hat{\omega}_{rk}\,\frac{R\nu_{ei}}{c_{sp}}\frac{1}{k_y\rho_{sp}} \tag{6}$$

We notice that the normalized wave number $k_y\rho_{sp}$ which is required to obtain (almost) the same growth rates and frequencies (in practice the same in the collisionless limit), that is, the same normalized $\hat{\gamma}_k$ and $\hat{\omega}_{rk}$ of the unstable mode, is not the same if we consider different H isotopes, but should correspond to the same $k_y\rho_i$, with $i$ the index which identifies the H

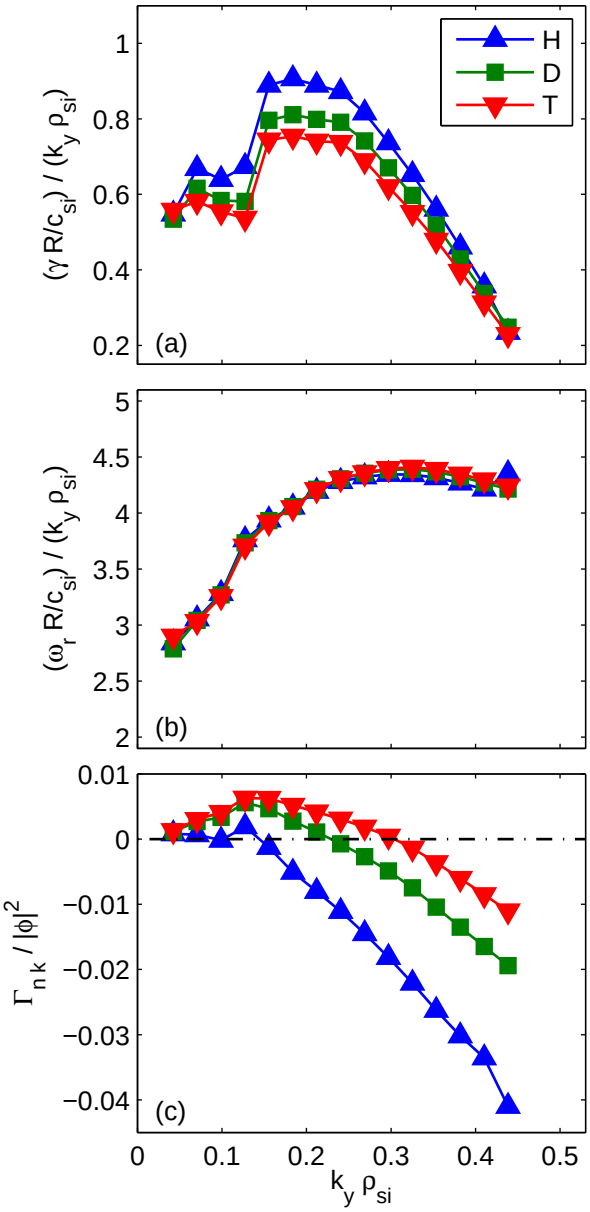


FIG. 1: (Color online) Spectrum of the normalized growth rate (a), real frequency (b) and quasi–linear particle flux as a function of the wave number for the three H isotopes

.

isotope, that $k_y\rho_{sp} = k_y\rho_{si}(m_p/m_i)^{0.5}$ [17]. This implies that the effect of the collisions on the turbulent particle convection becomes stronger with increasing isotope mass. The same result can also be obtained if we consider the expression of the fluid drift frequency $\omega_{Dk}$

which uses the main ion species parameters, $k_y \rho_{si} c_{si}/R$. In this case

$$\hat{\omega}_{rk}\,\hat{\nu}_k = \hat{\omega}_{rk}\,\frac{R\nu_{ei}}{c_{si}}\frac{1}{k_y\rho_{si}}, \tag{7}$$

and it is analogously easy to observe that since practically the same normalized growth rates and frequencies are obtained at the same $k_y\rho_i$, this term scales with the ratio of the collision frequency to the sound speed of the main ion species

$$\frac{\nu_{ei}R}{c_{si}} = \frac{R\,Z_i^2 e^4 \ln\Lambda_{ei}\,n_i}{4\pi\epsilon_0^2\,T_e^2}\,\left(\frac{m_i}{m_e}\right)^{1/2}.$$

We find that this term is proportional to the square root of the ion to electron mass ratio, and thereby increases with increasing isotope mass, consistent with the previous result. These two equivalent approaches also reflect two possible ways of setting the input when a different ion mass is considered in the numerical calculations with a gyrokinetic code. The latter is equivalent to use everytime the reference mass provided by the main ion isotope mass, and changing the correspondent relative mass of the electrons as input. The former is equivalent to using the same reference mass regardless the isotope mass of the main ion species, and **to change the normalized binormal wave number used as input in order to always obtain the same value of the product of the binormal wave number times the Larmor radius with the actual main ion mass**.

From a physical standpoint, this simple analytical derivation shows that with increasing isotope mass, the characteristic time for the perpendicular drift over a binormal wave length becomes relatively longer with respect to the characteristic collisional time (keeping fixed all other parameters and changing only the mass of the ions). The overall effect with respect to particle transport is that with increasing isotope mass the plasma behaves as if it were increasingly collisional, and thereby a stronger outward contribution to the turbulent convection is obtained with increasing isotope mass. At large collisionalities also the eigenvalues of the unstable mode start to be affected, particularly the growth rate (as, we anticipate, is clearly visible in Fig. 2 (a,b) in the numerical results presented in Section 2). In the case of ITG modes, the reduction of the growth rate produced by an increase of collisionality is definitely weaker than in the case of trapped electron modes (TEM), but can become significant at high collisionalities by reducing the destabilization of the ITG which is produced by the presence of trapped electrons. Consistent with previous results [17], we observe that the reduction of the growth rate is stronger with increasing mass of the hydrogen isotope,

as a consequence of the stronger impact of collisionality at lower isotope thermal velocity. Similarly, a stronger stabilization of the trapped electron mode (TEM) is obtained with increasing isotope mass [17, 20]. The same effect also implies that the (collisionless) curvature pinch, provided by the term $\hat{\gamma}_k \hat{\omega}_{dk}$ in Eq. (4), is reduced with increasing collisionality by the reduction of $\hat{\gamma}$ by an amount which increases with increasing mass of the isotope. The consequent reduction of the collisionless inward component of the convection with higher ion mass can increase the effect produced by the increase of the collisional outward component of the convection with increasing isotope mass, enhancing the effect of a more outward particle flux with increasing isotope mass.

While all of these collisional effects related to trapped particle convection imply that the radial particle flux is increasingly more outward with increasing mass of the hydrogen isotope, an opposite dependence can be produced by the convective contributions carried by the passing electrons. Particle transport mechanisms related to passing electron dynamics are usually not dominant, but, interestingly, their dependence on the isotope mass is also present in the collisionless limit. Eq. 5 shows that the entire passing particle flux is proportional to $c_s/v_{the}$, that is to $(m_e/m_i)^{0.5}$. We observe in particular that the passing electron dynamics produces a convective term proportional to $\hat{\omega}_r$, which is directed outward in ITG turbulence, that is with positive $\omega_r$, and which can offset the inward contribution produced by passing electron thermodiffusion depending on the relative size of $\hat{\omega}_r$ and $R/(2L_{Te})$.

Since both the convective and the diffusive terms of the passing particle flux have the same dependence on the ion mass, a change of the ion mass does not modify the value of $R/L_n$ at which the passing particle flux is equal to zero. However, when passing and trapped electron contributions are combined in the total particle flux, the different dependences on the ion mass of the passing and trapped particle fluxes (proportional to $(m_e/m_i)^{0.5}$ and independent of $(m_e/m_i)$ in the collisionless limit, respectively) imply that the value of $R/L_n$ at which the total particle flux is equal to zero can be modified. Under conditions where the total convection of passing electrons is outward (that is, in the presence of ITG turbulence with weak values of $R/L_{Te}$), the passing particle contribution can be such to produce an increase of the predicted value of $R/L_n$ at the null of the total particle flux with increasing mass of the isotope, that is an opposite dependence with respect to the one which is produced by collisions on the trapped particle flux only.

Finally, passing electrons and parallel dynamics also play a critical role in the more general

case of electromagnetic fluctuations. The analytical expression of the particle flux produced by passing electrons, Eq. 6 in [27], reveals that, at the leading order, terms at the numerator and the denominator are both proportional to $\sqrt{m_e/m_i}$, and thereby the electromagnetic component of the particle flux is weakly affected by a change of the ion mass.

In the next section, we show that all of these effects, as identified from the results of this analytical model, are reproduced in the numerical results provided by a gyrokinetic code. In particular, we expect that, for usual plasma parameters in the core of tokamaks, the dominant effect stems from the impact of collisions on the convection of trapped electrons, leading to the prediction that the normalized logarithmic density gradient $R/L_n$ at the null of the turbulent particle flux decrease with increasing hydrogen isotope mass, and with a difference among the isotopes which increases with increasing collisionality. Nonlinear numerical simulations will also allow us to quantitatively predict the magnitude of this effect.

## III. NUMERICAL RESULTS

Starting from the considerations allowed by the analytical model, a set of linear and nonlinear gyrokinetic simulations have been performed to compute the actual predicted magnitude of this effect. To this end we apply the gyrokinetic code GKW [22] and we consider typical plasma parameters of an H-mode plasma around mid–radius with $T_e = T_i$ at low edge safety factor. These conditions are expected to reproduce the conditions of the ITER baseline scenario [**28**] in the appropriate range of collisionality. In order to focus on the effects produced by the collisionality, we consider an electrostatic limit. The reference input parameters of these calculations are $T_e = T_i$, $R/L_{Te} = R/L_{Ti} = 6$, $r/R = 0.165$, $q = 1.13$, $\hat{s} = 0.6$. **A local Miller equilibrium [29] has been used. The complete list of input parameters is reported in Table I**.

The results presented in Fig. 1 compare the spectral properties of the quasi–linear particle flux produced by convective terms only, that is with $R/L_n = 0$ in the case of a H and a T plasma. These calculations include a relatively high collision frequency, corresponding to a major radius $R = 3$ m, density $n_e = 6\ 10^{19}$ m$^{-3}$ and temperature $T_e = 3$ keV. The spectrum of the growth rate and real frequencies for H and T are presented in Fig. 1(a) and (b), normalized to the corresponding $k_y \rho_{si} c_{si}/R$, with $\rho_{si} = c_{si}/\Omega_{ci}$ and $c_{si} = \sqrt{T_e/m_i}$. We observe

| Parameter | Value |
|---|---|
| r/R | 0.165 |
| local safety factor q | 1.13 |
| magnetic shear $\hat{s}$ | 0.60 |
| elongation $k$ | 1.41 |
| triangularity $\delta$ | 0.08 |
| squareness $\zeta$ | 0 |
| $(r/k)\, dk/dr$ | 0.047 |
| $(r/(1-\delta^2))\, d\delta/dr$ | 0.091 |
| $r d\zeta/dr$ | 0 |
| $dR/dr$ | -0.134 |
| $Z$ | 0 |
| $dZ/dr$ | 0 |
| $d\beta/dr$ | -0.25 |

TABLE I: Input parameters of the gyrokinetic calculations which describe the local Miller geometry

that similar normalized growth rates and almost the same frequencies are obtained when the spectra are plotted against the binormal wave number normalized to the Larmor radius of each main ion species. The small difference in the growth rate is due to the non-negligible stabilizing impact of the collisionality on the ITG growth rate in these conditions, and, consistent with the analysis presented in the previous section, it is stronger with increasing isotope mass (as also visible in Fig. 2(a,b)). The corresponding particle fluxes are presented in Fig. 1(c) and show an increase of the (convective) particle flux with increasing isotope mass in the outward (positive) direction at all wave numbers. A double scan in collision frequency and normalized logarithmic density gradient is performed. A subset of the results of this scan are presented in Fig. 2. The calculations are performed by considering the same reference mass $m_p$ regardless the value of the main ion mass. As a check of the proper implementation of the code, with respect to a correct inclusion of the terms involving the main ion mass, we have performed an additional set of calculations where the reference mass is considered to be equal to the main ion mass, obtaining identical results. For these linear calculations, a single characteristic wave number around the maximum growth rate has been

considered, that is $k_y\rho_{si} = 0.21$. This is equivalent to $k_y\rho_{sp} = 0.21$, to $k_y\rho_{sp} = 0.21/\sqrt{2}$ and to $k_y\rho_{sp} = 0.21/\sqrt{3}$ for H, D and T respectively, in order to obtain the same wave numbers normalized to the respective ion Larmor radii, where $\rho_{sp}$ is the Larmor radius corresponding to the proton mass. Correspondingly practically the same normalized growth rates (Fig 2a) and real frequencies (Fig. 2b) are obtained, regardless the isotope being used as main ion species in the calculations, with a small difference only appearing in the growth rates of the cases with the highest collisionality (corresponding to the collisionality of Fig. 1), and with lower growth rate in the case of T. In Fig. 2(c) the corresponding particle fluxes as a function of the logarithmic density gradient $R/L_n$ are plotted for the different collisionalities and the two isotopes, H and T, as identified in the legend. We observe that curves of the particle fluxes of H are more strongly inward at low values of $R/L_n$ and meet the condition of $\Gamma_n = 0$ at different values of $R/L_n$ with a difference which increases with increasing collisionality.

In Fig. 3 the results of Fig. 2 are summarized in terms of the dependence of the value of $R/L_n$ at the null of the particle flux ($\Gamma_n = 0$) as a function of the collision frequency for the three isotopes, demonstrating an increasing difference between H, D and T with increasing collisionality, consistent with the expected dependence obtained from the analysis of the analytical expression of the particle flux Eq. 4 presented in the previous section. The vertical lines in the figure identify the collisionality range of a low density, high power condition in present tokamaks (or, almost equivalently, of a high density, high power burning plasma in a reactor) (dashed) and the high collisionality range at intermediate to high density and power in present devices (dashed–dotted). We observe that in the range of operation of present tokamaks, that is for collisionalities larger than the dashed vertical line, H plasmas are expected to have measurably more peaked density profiles than the corresponding D (and T) plasmas.

While the radial flux of trapped electrons is usually largely dominant, it is interesting to also investigate the expected dependences of the passing particle flux by means of numerical calculations. To this end, we consider first an artificial situation in which both the electron temperature and the density logarithmic gradients are equal to zero, namely $R/L_{Te} = 0$ and $R/L_n = 0$, combined with $R/L_{Ti} = 9$ and a very small inverse aspect ratio $r/R = 10^{-4}$. Fig. 4 shows the particle flux as a function of the safety factor for different masses of the ion species (an A = 4 has been also included to more completely document the dependence) and demonstrate an almost exact proportionality to $(m_e/m_i)^{0.5}$ in the limit of small values of the

safety factor, that is for large values of $k_\parallel$, consistent with the limit under which the analytical formulae have been derived [23]. The particle flux, which in the limit of $R/L_{Te} = R/L_n = 0$ is made of a pure convective component only, is directed outwards, consistent with the analytical formula Eq. 5 for ITG modes. Due to the different dependences on the electron to ion mass ratio, the combination of trapped and passing particle fluxes is expexted to affect the value of $R/L_n$ at the null of the total particle flux. This effect is demonstrated in a set of linear gyrokinetic calculations with GKW in Fig. 5. The instability growth rates and frequencies are plotted in Fig. 5(a,c), and the corresponding particle fluxes are plotted in Fig. 5(b,d). We observe that depending on the input parameters, and in particular on the value of the electron temperature logarithmic gradient $R/L_{Te}$, the condition of particle flux equal to zero is met at different values of $R/L_n$ (Fig. 5b) or at the same values (Fig. 5d). The reason behind the different behaviour comes from the relative impact of trapped and passing particle contributions to the flux, where the passing particle flux component can be directed outward or inward depending on whether the value of $R/(2L_{Te})$ is respecticely larger or smaller than the normalized real frequency of the mode, as shown in the numerical results in Fig. 5, and consistent with the analytical result Eq. 5. For comparable electron and ion logarithmic temperature gradients, the trapped particle contribution largely dominates in the range of $R/L_n$ where the condition $\Gamma_n = 0$ is met, leading to a very weak dependence of $R/L_n$ on the mass at zero particle flux in the collisionless limit, as demonstrated in Fig. 3 and Fig. 5 for $R/L_{Te} = R/L_{Ti} = 6$ and $R/L_{Te} = R/L_{Ti} = 9$ respectively.

In contrast, when $R/L_{Te}$ is smaller (Fig. 5b), the condition $\Gamma_n = 0$ is met at values of $R/L_n$ where the passing particle contribution is still significant, leading to values of $R/L_n$ at $\Gamma_n = 0$ which are larger with increasing mass of the ion. The difference between the curves for the hydrogen isotopes increases with decreasing $\epsilon = r/R$, that is with increasing fraction of passing particles. It has also been verified that this difference increases with decreasing safety factor, consistent with the analytical formula Eq. (5), for which an enhancement of the passing particle flux is obtained with a reduction of the parallel wave number $k_\parallel \propto 1/(qR)$.

A set of nonlinear gyrokinetic simulations have been performed to more precisely quantify these effects. The same reference input parameters as in the linear calculations presented in Figs. (1-3) have been applied, namely $T_e = T_i$, $R/L_{Te} = R/L_{Ti} = 6$ and same geometrical parameters, which represent typical conditions around mid–radius. Four nonlinear simulations have been performed at the two collisionality values identified by vertical lines in Fig.

3, corresponding to collisionality factors $\overline{\nu} = Rn_e/T_e^2$ equal to 0.2 and 2. Correspondingly two different values of $R/L_n$ have been used at each collisionality and for each H isotope in order to identify the corresponding values of $R/L_n$ at which the condition $\Gamma_n = 0$ is fullfilled for H and T in the nonlinear results.

All of these nonlinear simulations use a box in the radial direction $L_x/\rho_{si} = 124.4$ and in the binormal direction $L_y/\rho_{si} = 149.2$, with 43 toroidal mode numbers and 339 radial mode numbers, resolving from $k_y\rho_{si} = 0.0421$ to $k_y\rho_{si} = 1.77$ and from $k_x\rho_i = 0.0438$ to $k_x\rho_i = 7.40$, and 32 points in the parallel direction have been considered. The velocity space is discretized in parallel velocity, with 64 grid points, and magnetic moment, with 16 grid points. All of the nonlinear simulations have been performed considering that the reference mass is the mass of the main ion, thereby ensuring that exactly the same domain and resolution are used when changing the main ion mass, that is, the only input parameter which is changed is the ratio of the electron mass to the reference mass. The first interesting result which is provided by the nonlinear simulations is a comparison of the nonlinear spectra, when only the mass of the H isotope is changed. In Fig. 6 the nonlinear spectra of the electrostatic potential fluctuations (a,c) and of the particle fluxes (b,d) obtained at the two selected collisionalities $Rn_e/T_e^2 = 0.2$ and 2 are compared for two corresponding values of $R/L_n = 2.5$ and 1.5 respectively, at which the particle flux for the H case is very close to zero. We observe that the change in main ion mass from H to T produces spectra of electrostatic potential fluctuations that almost exactly scale proportional to $v_{thH}/v_{thi} = A^{1/2}$, as expected from the gyro–Bohm nature of these electrostatic simulations without any $E \times B$ shearing. In constrast, the corresponding particle fluxes exhibit very strong differences, which become larger in the more collisional case. We recall that the effect of collisions on the particle flux spectrum is stronger at smaller wave numbers [24], leading to a particle flux which is more outward at small wave numbers with respect to the corresponding collisionless case. Thereby with increasing collisionality the wave numbers at which the particle flux spectrum remains negative become increasingly larger. The same happens due to an increase of the main ion mass, as shown in Fig. 3(c,d), which clarifies the similarity with an increase of the effective collisionality. We also observe that while in the case at lower collisionality the particle flux spectrum of the T case is still clearly negative in a range of sufficiently large wave numbers, the case at higher collisionality exhibit a particle flux spectrum in the T case which is almost entirely positive. The nonlinear results obtained for H and T at these

two values of collisionality are presented in Fig. 7(a), where the particle fluxes are plotted as a function of $R/L_n$. This allows us to identify the values of $R/L_n$ which correspond to the condition of zero flux. These values are then plotted as a function of the collisionality parameter $\overline{\nu} = Rn_e/T_e^2$ in Fig. 5(b). This demonstrates that the nonlinear results are consistent with the trends produced by the quasi–linear results presented in Fig. 3 and shows that in the collisionality range of present tokamaks this collisionality induced effect can produce differences between the normalized logarithmic density gradient of H plasmas and that of T plasmas which are as large as $\Delta R/L_n \simeq 1$. In contrast, this mechanism can be expected to not produce any measurable difference at the low collisionality of a fusion reactor.

## IV. QUALITATIVE COMPARISON WITH EXPERIMENTAL OBSERVATIONS IN JET AND AUG

In this section we investigate whether a qualitative evidence of a difference in the peaking between the density profiles of H and D plasmas is present in the observations of the AUG and the JET experiments. In order to focus on effects produced by turbulence convection only we consider plasmas with only one positive ion neutral injector (PINI) of the neutral beam injection (NBI) system at JET and without NBI at AUG, thereby with small to neglible particle source in the core and low toroidal rotation. All of these plasma phases are in low confinement (L–) mode. We have compiled two databases of stationary phases in H and D discharges, one for each device, and identified pairs of shots which allow more direct comparisons of the profiles. In this section we show scatter plots of the normalized logarithmic density gradient $R/L_n$ as a function of the collisionality parameter $\overline{\nu} = Z_{\rm eff} Rn_e/T_e^2$ for the two devices. We start this section by showing the comparison of the density profiles of a specific pair of H and D discharges from a dedicated AUG experiment in which auxiliary heating powers were adjusted to obtain a good match of the electron and ion temperature profiles in H and D, at the same densities [13]. The density profiles corresponding to the best match, largely analyzed in [13], are presented in Fig. 8(a), and a comparison of the respective normalized logarithmic density gradient profiles is presented in Fig. 8(b). The measurements provide some evidence that in these matched conditions the density profile of the H plasma in the core region is slightly more peaked than that of the corresponding D

plasma, with a difference in the normalized logarithmic density gradient which is approximately consistent with the theoretical expectations with the collisionality parameter of this L–mode plasma, $Z_{\rm eff} R n_e / T_e^2 \simeq 25$. Both these H and D plasmas exhibit low effective charge numbers in the core region, below 1.5 (around 1.2 at mid–radius) and with no significant difference between H and D. At the edge, the D plasma has a $Z_{\rm eff}$ reaching 2, and larger than the corresponding H plasma, in which $Z_{\rm eff}$ remains below 1.5. This type of comparison has been extended to a dataset of AUG plasmas with electron cyclotron heating only. The complete list of AUG discharge numbers, selected time for the analysis, and usual global parameters is presented in Tables II and III in the Appendix for D and H plasmas respectively. The scatter plots of the normalized logarithmic density gradient in a radial window representative of the core confinement region as a function of the collisionality parameter and of the ratio of the electron to ion stored energy are presented in Fig. 9 (a,b) respectively (since a significant fraction of these plasmas does not have ion temperature measurements, the ratio of the electron to ion stored energy is used as a proxy of the volume averaged electron to ion temperature ratio). In the case of this AUG L–mode dataset, the collisionality parameter does not order the points, as conditions of strong electron heating lead to flatter profiles, as indicated by the scatter plot as a function of the electron to ion stored energy ratio. However, it can be observed that in these conditions which are completely free of a particle source in the core, the density profiles of the H plasmas exhibit logarithmic density gradients which are slightly more peaked than the D plasmas at the same collisionality or at the same ratio of the electron to ion stored energy. **Since ion temperature measurements are not available for most of the points, the thermal stored energy of the electrons has been obtained from the measured electron kinetic profiles, and that of the ions has been computed subtracting the electron stored energy from the total stored energy provided by the magnetic measurements (there are no beam ions in these plasmas).**

A data set of JET observations has also been built in order to perform a similar comparison on JET plasmas. These plasma have currents around 2 MA, and magnetic fields from 3.1 and 3.3 T. Auxiliary heating is provided by a maximum of a single NBI PINI, and additional ICRH power from 1.5 MW to 5 MW, with different heating schemes producing dominant ion (at low $He^3$ minority concentration) and electron (in mode conversion at higher $He^3$ minority concentration) heating. The complete list of JET discharge numbers,

selected time for the analysis, and usual global parameters is presented in Tables IV and V in the Appendix for D and H plasmas respectively. Measurements of the electron density and temperature are taken by the High Resolution Thomson Scattering (HRTS) diagnostics. The scatter plot of the normalized logarithmic density gradient of JET H and D plasmas as a function of the collisionality parameter $Z_{\rm eff}Rn_e/T_e^2$ is presented in Fig. 10. Due to the lower energy confinement of H plasmas, the collisionality windows of the plasmas in D and H do not completely overlap, as H plasmas are more collisional than the D plasmas. The collisionality parameter orders the density peaking of these plasmas sufficiently well. This observation is presented here for the first time in L–mode plasmas at JET, and it is complementary to previous studies pointing out a dominant dependence on the peaking of the current density profile in L–mode plasmas with off–axis lower hybrid heating and current drive only [30]. An analogous collisionality dependence of the density peaking in L–mode plasmas was pointed out in AUG [31]. The observed collisionality dependences in H and D plasmas suggest trends by which only a weak evidence can be obtained of a stronger peaking of H plasmas than the D plasmas at the same collisionality, or, at least, one can state that no evidence outside experimental error bars is obtained which is in clear disagreement with the theoretical results. It is important also to add that a larger difference in line averaged $Z_{\rm eff}$ values between D and H is obtained from measurements at JET as compared to AUG, with D plasmas usually exhibiting $Z_{\rm eff}$ values which exceed those of the H plasmas by about $\Delta Z_{\rm eff} \simeq 0.5$. Whether this difference is only peripheral or also significant in the core region of the plasma is however unclear. If it is assumed that also at JET the difference between the $Z_{\rm eff}$ values remains limited in the core of D and H plasmas, as observed in AUG, then a somewhat clearer evidence of an increased peaking of the density in H plasmas as compared to D plasmas at the same collisionality is obtained. A companion analysis of JET Ohmic plasmas in D and in H did not allow us to draw any clear conclusion either, outside the experimental uncertainties, for the validation (or invalidation) of the theoretical results. The uncertainties and potential differences in $Z_{\rm eff}$ values, and impurity content more in general, in otherwise similar H and D plasmas it is an additional interesting topic for experimental investigation, which is however left for future work. This might also impact the conclusions of the present study regarding the differences between the density peaking in H and D plasmas at the same collisionality, which are in any case predicted to be relatively small by the theory.

## V. CONCLUSIONS

The impact of the change of the mass of the ion species, as in plasmas with different hydrogen isotopes, on the turbulent particle flux has been investigated from the theoretical standpoint by making use of analytical formulae derived from the gyrokinetic equation and numerical results from both linear and nonlinear simulations with the gyrokinetic code GKW. The dominant mechanism leading to a change of the particle flux and thereby producing a modification of the logarithmic density gradient at the condition where the particle flux is equal to zero has been found to be provided by the component of the trapped particle convection induced by collisions. This convective contribution is directed outward in ion temperature gradient turbulence, increases with increasing collisionality, and is proportional to the square root of the ion mass, keeping all other parameters the same. Thereby, it leads to the prediction of an increasing logarithmic gradient of the electron density, with decreasing mass of the hydrogen isotope. Nonlinear gyrokinetic simulations with typical parameters around mid–radius have shown that this effect can produce measurable differences, particularly when comparing H and T. In the collisionless limit this effect vanishes, and for usual plasma parameters in the confinement region no significant difference is predicted among the logarithmic density profiles of plasmas with different hydrogen isotopes as ion species. Passing electrons also contribute a usually subdominant component of the particle flux, which is proportional to the inverse of the square root of the ion mass. While alone this dependence does not produce any modification of the value of the logarithmic density gradient at the null of the flux, when combined with the trapped particle component, it can have an effect, also in the collisionless limit. Consistent with the analytical results, it has been shown that the sign of this contribution depends on the relative size of the electron temperature gradient and the normalized real frequency of the unstable mode, and it is directed outward in conditions of ITG turbulence with weak electron temperature gradients, whereas it can become inward with increasingly large electron temperature gradients, or in trapped electron mode turbulence. At usual parameters around mid–radius, with comparable electron and ion temperature gradients, these effects turn out to compensate and to provide a practically negligible modification to the value of the logarithmic density gradient at zero particle flux.

These theoretical results lead to the expectation that the peaking of the density profiles of H plasmas be slightly higher than those of D plasmas, at similar plasma parameters

and without a significant particle source, with a difference that increases with increasing collisionality of the plasma and vanishes at the low collisionality expected in a reactor burning plasma. Available measurements of plasma kinetic profiles from recent AUG and JET experiments in L-mode, respectively without or with a small central particle source, show that the density profiles of H and D plasmas are usually very similar. While it has been difficult to find a large amount of otherwise perfectly matched conditions, due to the usual lower confinement in H leading to a higher collisionality, evidence of a slightly larger peaking of the density profiles in H as compared to those in D has been obtained in an otherwise matched pair of plasmas in AUG [13]. While the difference is at the limit of the experimental uncertainties, analysis of a larger dataset of plasmas (although without close match of parameters) provides indications which are consistent with this observation. In obtaining this result, it has been observed that significant differences in $Z_{\rm eff}$ profiles measured in H and D plasmas in AUG are only obtained at the periphery of the plasma.

An analogous analysis dedicated to JET plasmas in L–mode with a maximum of one positive ion neutral injector of the NBI system shows an overall clear trend of decreasing density peaking with increasing collisionality, but provides a weak evidence only of a difference between H and D plasmas which can be considered outside the error bars. In contrast to AUG plasmas, at JET significantly higher values of $Z_{\rm eff}$ are measured in D plasmas as compared to H plasmas, but it remains unclear how much this difference is coming from the periphery of the plasma only. If it is assumed that also at JET the $Z_{\mathbf{eff}}$ values do not exhibit a significant difference in the central region of H and D plasmas, then a clearer evidence of a higher density peaking in H plasmas as compared to D plasmas at the same collisionality could be obtained.

The theoretical results of this work could motivate further experimental investigations, with also the inclusion of T plasmas, as planned in the forthcoming experimental campaigns at JET, for which a larger difference as compared to H plasmas is predicted.

## VI. APPENDIX: TABLES OF EXPERIMENTAL OBSERVATIONS

In order to provide complete information and traceability, in Tables II to V we provide the list of plasma discharges and selected time slices used for the analysis, as well as the main global plasma parameters respectively for AUG (Tables II and III) and JET (Tables

| AUG# | main ion | time [s] | $I_p$ [MA] | $B$ [T] | $q_{95}$ | $n_{el}$ [$10^{19}$ m$^{-3}$] | $P_{ECRH}$ [MW] |
|---|---|---|---|---|---|---|---|
| 23091 | D | 1.85 | 1.00 | 2.53 | 4.2 | 1.93 | 0.71 |
| 23266 | D | 1.65 | 1.00 | 2.29 | 4.0 | 1.98 | 0.52 |
| 23266 | D | 2.35 | 1.00 | 2.29 | 4.0 | 1.93 | 1.28 |
| 23267 | D | 1.65 | 1.00 | 2.29 | 4.0 | 1.98 | 0.57 |
| 23268 | D | 1.65 | 1.00 | 2.29 | 4.0 | 2.00 | 0.58 |
| 23270 | D | 1.57 | 1.00 | 2.29 | 4.0 | 1.98 | 0.01 |
| 23270 | D | 2.10 | 1.00 | 2.29 | 4.0 | 1.93 | 1.37 |
| 23270 | D | 2.80 | 1.00 | 2.29 | 4.0 | 2.06 | 1.43 |
| 23271 | D | 1.57 | 1.00 | 2.29 | 4.0 | 1.96 | 0.59 |
| 23271 | D | 2.10 | 1.00 | 2.29 | 4.0 | 1.95 | 1.36 |
| 23271 | D | 2.80 | 1.00 | 2.29 | 4.0 | 2.05 | 1.43 |
| 23366 | D | 2.85 | 1.00 | 2.25 | 3.9 | 1.91 | 2.04 |
| 23092 | D | 2.95 | 1.00 | 2.53 | 4.4 | 2.40 | 0.72 |
| 23266 | D | 3.62 | 1.00 | 2.29 | 4.0 | 2.40 | 1.27 |
| 23268 | D | 3.55 | 1.00 | 2.29 | 4.1 | 2.38 | 1.26 |
| 23270 | D | 3.55 | 1.00 | 2.29 | 4.0 | 2.37 | 1.43 |
| 23271 | D | 3.55 | 1.00 | 2.29 | 4.0 | 2.34 | 1.43 |
| 23272 | D | 1.57 | 1.00 | 2.29 | 4.0 | 2.49 | 0.51 |
| 23272 | D | 2.15 | 1.00 | 2.29 | 4.0 | 2.40 | 1.15 |
| 27805 | D | 3.45 | 1.00 | 2.48 | 4.2 | 2.44 | 0.89 |
| 27806 | D | 3.20 | 1.00 | 2.48 | 4.1 | 2.43 | 1.32 |
| 27806 | D | 3.90 | 1.00 | 2.48 | 4.2 | 2.42 | 0.80 |
| 27807 | D | 2.90 | 1.00 | 2.48 | 4.1 | 2.49 | 1.31 |
| 27810 | D | 3.10 | 1.00 | 2.48 | 4.2 | 2.42 | 0.91 |
| 27811 | D | 3.10 | 1.00 | 2.48 | 4.2 | 2.44 | 1.10 |
| 23272 | D | 2.85 | 1.00 | 2.29 | 4.0 | 2.85 | 1.23 |
| 26994 | D | 3.30 | 1.00 | 2.43 | 4.0 | 2.75 | 0.32 |
| 26994 | D | 4.30 | 1.00 | 2.43 | 4.1 | 2.77 | 0.33 |
| 27126 | D | 3.50 | 0.99 | 2.43 | 4.0 | 3.83 | 0.02 |
| 30690 | D | 2.00 | 0.80 | 2.47 | 5.4 | 4.12 | 0.50 |
| 30690 | D | 4.00 | 0.80 | 2.47 | 5.3 | 4.27 | 0.52 |
| 30692 | D | 2.00 | 0.80 | 2.46 | 5.2 | 4.21 | 0.51 |
| 30692 | D | 4.00 | 0.80 | 2.46 | 5.2 | 4.23 | 0.49 |
| 30693 | D | 2.00 | 0.80 | 2.46 | 5.1 | 4.14 | 0.49 |
| 30693 | D | 4.00 | 0.80 | 2.46 | 5.0 | 4.30 | 0.49 |
| 30694 | D | 2.00 | 0.80 | 2.45 | 5.0 | 4.14 | 0.50 |
| 30694 | D | 4.00 | 0.80 | 2.45 | 5.0 | 4.28 | 0.49 |

TABLE II: AUG discharge number with D as main ion H isotope, reference time, and corresponding plasma current, magnetic field, edge safety factor, line averaged density, and ECRH power that have been used in this paper and presented in Fig. 9

.

IV and V), with D (Tables II and IV) and H (Tables III and V) as main ion species, that have been used in the present study.

**Acknowledgments** This work has been carried out within the framework of the EUROfusion Consortium and has received funding from the Euratom research and training programme 2014-2018 under grant agreement No 633053. The views and opinions expressed

| AUG# | main ion | time [s] | $I_p$ [MA] | $B$ [T] | $q_{95}$ | $n_{el}$ [$10^{19}$ m$^{-3}$] | $P_{ECRH}$ [MW] |
|---|---|---|---|---|---|---|---|
| 27370 | H | 2.00 | 1.00 | -2.30 | -3.6 | 2.01 | 1.39 |
| 27370 | H | 2.55 | 1.00 | -2.30 | -3.7 | 1.97 | 2.12 |
| 31739 | H | 1.95 | 1.00 | -2.46 | -4.1 | 2.34 | 0.53 |
| 31739 | H | 2.65 | 1.00 | -2.46 | -4.0 | 2.33 | 1.16 |
| 31739 | H | 3.45 | 1.00 | -2.46 | -4.0 | 2.28 | 1.87 |
| 31739 | H | 4.55 | 1.00 | -2.46 | -4.0 | 2.30 | 1.95 |
| 31741 | H | 1.95 | 1.00 | -2.48 | -4.1 | 2.36 | 0.53 |
| 31741 | H | 2.65 | 1.00 | -2.48 | -4.0 | 2.35 | 1.12 |
| 31741 | H | 3.65 | 1.00 | -2.48 | -4.0 | 2.30 | 1.92 |
| 31741 | H | 5.50 | 1.00 | -2.48 | -4.0 | 2.32 | 0.56 |
| 31740 | H | 1.95 | 1.00 | -2.47 | -4.1 | 2.83 | 0.52 |
| 31740 | H | 2.65 | 1.00 | -2.47 | -4.0 | 2.84 | 1.17 |
| 31740 | H | 5.40 | 1.00 | -2.47 | -4.0 | 2.86 | 0.54 |
| 27367 | H | 1.83 | 0.99 | -2.29 | -3.7 | 3.97 | 1.45 |
| 27367 | H | 2.11 | 1.00 | -2.29 | -3.7 | 3.81 | 0.75 |
| 27367 | H | 2.54 | 1.00 | -2.29 | -3.8 | 3.90 | 1.40 |
| 27367 | H | 2.91 | 1.00 | -2.29 | -3.8 | 3.95 | 1.20 |
| 27368 | H | 2.00 | 1.00 | -2.29 | -3.6 | 3.96 | 1.40 |
| 27368 | H | 2.55 | 1.00 | -2.29 | -3.8 | 3.90 | 2.13 |
| 31364 | H | 2.00 | 0.80 | -2.49 | -4.9 | 4.07 | 0.49 |
| 31364 | H | 4.00 | 0.81 | -2.49 | -4.9 | 4.27 | 0.62 |
| 31366 | H | 2.00 | 0.80 | -2.49 | -4.9 | 4.23 | 0.81 |
| 31366 | H | 4.00 | 0.81 | -2.48 | -4.9 | 4.27 | 0.79 |
| 31369 | H | 2.00 | 0.80 | -2.49 | -4.9 | 4.23 | 0.83 |
| 31369 | H | 4.00 | 0.81 | -2.48 | -4.9 | 4.31 | 0.81 |
| 31370 | H | 2.00 | 0.80 | -2.49 | -4.9 | 4.23 | 0.82 |
| 31370 | H | 4.00 | 0.81 | -2.48 | -4.9 | 4.28 | 0.80 |

TABLE III: AUG discharge number with H as main ion H isotope, reference time, and corresponding plasma current, magnetic field, edge safety factor, line averaged density, and ECRH power that have been used in this paper and presented in Fig. 9

.

herein do not necessarily reflect those of the European Commission. The nonlinear gyrokinetic simulations were performed on the parallel server Hydra of the Max–Planck Computing and Data Facility, Garching, Germany. The Authors are grateful to Benedikt Geiger, Rainer Fischer and Bernd Kurzan for their support with the analysis of the ASDEX Upgrade density profile and effective charge measurements, and to Anthony Shaw for the analysis of the effective charge measurements at JET. The Authors are also grateful to Costanza Maggi, Ephrem Delabie and Nicola Bonanomi for very fruitful discussions.

[1] ASDEX Team Nucl. Fusion **29** 1959 (1989).

| JET# | main ion | time [s] | $I_p$ [MA] | $B$ [T] | $q_{95}$ | $n_{el}$ [$10^{19}$ m$^{-3}$] | $P_{NBI}$ [MW] | $P_{ICRH}$ [MW] |
|---|---|---|---|---|---|---|---|---|
| 90668 | D | 49.00 | 1.98 | 3.29 | 5.0 | 2.65 | 1.65 | 2.77 |
| 90671 | D | 49.00 | 1.98 | 3.29 | 5.0 | 2.67 | 1.54 | 2.71 |
| 77445 | D | 49.00 | 1.78 | 3.33 | 6.1 | 2.07 | 1.27 | 2.40 |
| 77446 | D | 49.00 | 1.78 | 3.33 | 6.1 | 2.21 | 1.27 | 4.29 |
| 77447 | D | 49.00 | 1.79 | 3.33 | 6.1 | 2.21 | 1.27 | 5.70 |
| 77451 | D | 49.00 | 1.78 | 3.33 | 6.2 | 2.21 | 1.26 | 6.14 |
| 90672 | D | 49.00 | 1.98 | 3.29 | 5.0 | 2.50 | 1.53 | 6.45 |
| 90670 | D | 49.00 | 1.98 | 3.29 | 5.0 | 2.54 | 1.54 | 6.01 |
| 90669 | D | 49.00 | 2.04 | 3.39 | 5.0 | 2.53 | 1.63 | 5.35 |
| 90666 | D | 49.00 | 1.98 | 3.29 | 5.0 | 2.54 | 1.65 | 4.77 |
| 89983 | D | 50.00 | 1.96 | 3.04 | 4.5 | 2.31 | 2.28 | 0.31 |
| 88556 | D | 50.00 | 1.81 | 3.12 | 4.6 | 2.63 | 0.00 | 4.27 |
| 88551 | D | 56.00 | 1.79 | 3.05 | 4.6 | 2.52 | 0.00 | 2.10 |
| 88552 | D | 56.00 | 1.79 | 3.05 | 4.6 | 2.47 | 0.00 | 2.69 |
| 88553 | D | 56.00 | 1.79 | 3.05 | 4.6 | 2.52 | 0.00 | 3.02 |
| 88554 | D | 50.00 | 1.81 | 3.12 | 4.6 | 2.57 | 0.00 | 3.88 |
| 88527 | D | 54.00 | 1.79 | 3.32 | 5.0 | 2.67 | 0.00 | 0.52 |
| 88528 | D | 54.00 | 1.79 | 3.32 | 5.0 | 2.69 | 0.00 | 1.03 |
| 88529 | D | 54.00 | 1.79 | 3.05 | 4.6 | 2.55 | 0.00 | 1.98 |
| 88530 | D | 54.00 | 1.79 | 3.05 | 4.6 | 2.60 | 0.00 | 2.52 |
| 88532 | D | 54.00 | 1.79 | 3.05 | 4.6 | 2.57 | 0.00 | 2.48 |
| 88533 | D | 54.00 | 1.79 | 3.05 | 4.6 | 2.55 | 0.00 | 2.45 |
| 88534 | D | 54.00 | 1.79 | 3.05 | 4.6 | 2.54 | 0.00 | 2.01 |
| 88511 | D | 54.00 | 1.79 | 3.32 | 5.0 | 2.59 | 0.00 | 0.26 |
| 88515 | D | 54.00 | 1.79 | 3.32 | 5.0 | 2.60 | 0.00 | 1.02 |
| 88467 | D | 54.00 | 1.80 | 3.32 | 5.8 | 2.97 | 0.00 | 0.30 |
| 88468 | D | 54.00 | 1.80 | 3.32 | 5.8 | 2.92 | 0.00 | 0.14 |
| 88419 | D | 51.00 | 1.65 | 3.23 | 5.9 | 2.47 | 0.00 | 0.00 |
| 78807 | D | 51.00 | 1.78 | 3.31 | 6.3 | 2.19 | 1.33 | 3.90 |
| 78808 | D | 50.00 | 1.78 | 3.31 | 6.1 | 2.05 | 1.33 | 0.00 |
| 78802 | D | 51.00 | 1.78 | 3.31 | 6.3 | 2.20 | 1.41 | 3.90 |
| 78804 | D | 51.00 | 1.79 | 3.31 | 6.6 | 2.42 | 1.42 | 3.90 |
| 78797 | D | 50.00 | 1.78 | 3.31 | 6.3 | 2.23 | 1.24 | 2.92 |
| 78798 | D | 50.00 | 1.78 | 3.31 | 6.3 | 2.20 | 1.33 | 4.88 |
| 78799 | D | 50.00 | 1.78 | 3.31 | 6.3 | 2.18 | 1.33 | 3.90 |
| 92247 | D | 53.00 | 1.66 | 2.98 | 4.8 | 2.52 | 1.92 | 0.00 |
| 92248 | D | 53.00 | 1.66 | 2.98 | 4.8 | 2.47 | 1.78 | 0.00 |
| 92249 | D | 53.00 | 1.66 | 2.98 | 4.8 | 2.62 | 1.78 | 0.00 |
| 92250 | D | 53.00 | 1.66 | 2.98 | 4.8 | 2.55 | 1.73 | 0.00 |
| 78830 | D | 49.00 | 2.28 | 3.42 | 5.0 | 2.01 | 0.00 | 1.20 |
| 78831 | D | 49.00 | 1.78 | 3.42 | 6.5 | 2.00 | 0.00 | 1.23 |
| 78825 | D | 49.00 | 2.77 | 3.42 | 4.1 | 2.00 | 0.00 | 2.02 |
| 78840 | D | 49.00 | 2.94 | 3.41 | 3.8 | 1.98 | 0.00 | 0.99 |
| 78843 | D | 49.00 | 2.77 | 3.41 | 4.1 | 2.08 | 0.00 | 2.19 |
| 78844 | D | 49.00 | 2.77 | 3.41 | 4.1 | 2.09 | 0.00 | 1.18 |
| 78845 | D | 49.00 | 2.77 | 3.41 | 4.1 | 2.12 | 0.00 | 2.45 |
| 78847 | D | 49.00 | 2.77 | 3.41 | 4.1 | 2.05 | 0.00 | 1.89 |
| 78848 | D | 49.00 | 1.78 | 3.41 | 6.4 | 2.15 | 0.00 | 2.99 |
| 78834 | D | 49.00 | 1.78 | 3.42 | 6.5 | 2.02 | 0.00 | 1.48 |
| 77440 | D | 49.00 | 1.63 | 3.33 | 6.2 | 2.21 | 1.18 | 2.49 |
| 77443 | D | 49.00 | 1.78 | 3.33 | 6.1 | 2.02 | 1.26 | 2.61 |

TABLE IV: JET discharge number with D as main ion H isotope, reference time, and corresponding plasma current, magnetic field, edge safety factor, line averaged density, and ECRH power that have been used in this paper and presented in Fig. 10



.

| JET# | main ion | time [s] | $I_p$ [MA] | $B$ [T] | $q_{95}$ | $n_{el}$ [$10^{19}$ m$^{-3}$] | $P_{NBI}$ [MW] | $P_{ICRH}$ [MW] |
|---|---|---|---|---|---|---|---|---|
| 91626 | H | 49.00 | 1.97 | 3.28 | 4.9 | 2.24 | 0.72 | 3.63 |
| 91322 | H | 49.00 | 1.77 | 3.15 | 5.6 | 3.09 | 0.71 | 2.22 |
| 91319 | H | 51.00 | 1.77 | 3.16 | 5.6 | 3.22 | 0.68 | 2.37 |
| 91315 | H | 50.80 | 1.71 | 3.16 | 5.8 | 2.78 | 0.00 | 0.00 |
| 91300 | H | 50.00 | 1.77 | 3.17 | 5.6 | 2.31 | 0.00 | 4.10 |
| 91301 | H | 52.00 | 1.77 | 3.16 | 5.5 | 2.48 | 0.00 | 4.65 |
| 91302 | H | 49.00 | 1.75 | 3.17 | 5.5 | 2.93 | 0.00 | 1.81 |
| 91302 | H | 51.00 | 1.76 | 3.16 | 5.4 | 2.86 | 0.00 | 3.61 |
| 91302 | H | 53.00 | 1.76 | 3.16 | 5.4 | 2.82 | 0.00 | 5.40 |
| 91296 | H | 50.00 | 1.96 | 3.26 | 5.2 | 2.64 | 0.00 | 2.05 |
| 91296 | H | 51.50 | 1.96 | 3.26 | 5.2 | 2.67 | 0.00 | 2.82 |
| 91296 | H | 52.80 | 1.95 | 3.26 | 5.3 | 3.04 | 0.00 | 0.00 |
| 91296 | H | 54.00 | 1.96 | 3.26 | 5.2 | 2.72 | 0.00 | 2.04 |
| 91296 | H | 56.30 | 1.96 | 3.26 | 5.2 | 2.80 | 0.00 | 2.81 |
| 91297 | H | 50.00 | 1.96 | 3.26 | 5.2 | 2.66 | 0.00 | 2.09 |
| 91297 | H | 51.50 | 1.96 | 3.25 | 5.2 | 2.73 | 0.00 | 3.32 |
| 91297 | H | 52.80 | 1.95 | 3.26 | 5.3 | 3.13 | 0.00 | 0.00 |
| 91297 | H | 54.00 | 1.96 | 3.25 | 5.2 | 2.69 | 0.00 | 2.09 |
| 91298 | H | 50.00 | 1.96 | 3.27 | 5.2 | 2.50 | 0.00 | 2.09 |
| 91298 | H | 51.50 | 1.96 | 3.26 | 5.2 | 2.67 | 0.00 | 3.27 |
| 91298 | H | 52.80 | 1.95 | 3.26 | 5.3 | 2.88 | 0.00 | 0.00 |
| 91298 | H | 54.00 | 1.96 | 3.26 | 5.2 | 2.60 | 0.00 | 2.09 |
| 91146 | H | 50.00 | 1.81 | 2.98 | 4.7 | 2.14 | 0.00 | 0.18 |
| 91147 | H | 50.00 | 1.81 | 2.98 | 4.7 | 2.13 | 0.00 | 0.33 |
| 91148 | H | 50.00 | 1.81 | 2.98 | 4.7 | 2.17 | 0.00 | 0.57 |
| 91149 | H | 50.00 | 1.81 | 2.98 | 4.7 | 2.22 | 0.00 | 1.16 |
| 91150 | H | 50.00 | 1.80 | 2.64 | 3.6 | 2.16 | 0.00 | 0.00 |
| 91152 | H | 49.50 | 1.81 | 3.08 | 4.9 | 2.24 | 0.00 | 2.43 |
| 91153 | H | 49.50 | 1.81 | 2.98 | 4.7 | 2.29 | 0.00 | 1.82 |
| 91154 | H | 49.50 | 1.82 | 2.98 | 4.7 | 2.23 | 0.00 | 2.02 |
| 91155 | H | 49.50 | 1.82 | 2.98 | 4.7 | 2.25 | 0.00 | 2.36 |
| 91705 | H | 49.00 | 1.87 | 3.08 | 4.9 | 2.50 | 0.69 | 1.37 |
| 91706 | H | 49.00 | 1.87 | 3.03 | 4.8 | 2.52 | 0.69 | 2.75 |
| 91708 | H | 49.00 | 1.87 | 3.03 | 4.8 | 2.42 | 0.72 | 2.75 |
| 91625 | H | 49.00 | 1.97 | 3.28 | 4.9 | 2.26 | 0.72 | 3.64 |

TABLE V: JET discharge number with H as main ion H isotope, reference time, and corresponding plasma current, magnetic field, edge safety factor, line averaged density, and ECRH power that have been used in this paper and presented in Fig. 10

.


[2] M. Bessenrodt-Weberpals, F. Wagner, O. Gehre, L. Giannone, J. V. Hofmann, A. Kallenbach, K. McCormick, V. Mertens, H. D. Murmann, F. Ryter, B. D. Scott, G. Siller, F. X. Soldner, A. Stabler, K.-H. Steuer, U. Stroth, N. Tsois, H. Verbeek and H. Zohm, Nucl. Fusion **33** 1205 (1993).

[3] D. P. Schissel, K. H. Burrell, J. C. DeBoo, R. J. Groebner, A. G. Kellman, N. Ohyabu, T. H. Osborne, M. Shimada1, R. T. Snider, R. D. Stambaugh, T. S. Taylor and DIII-D Research

Team, Nucl. Fusion **29** 185 (1989).

[4] F. Tibone, B. Balet, M. Bures, J. G. Cordey, T. T. C. Jones, P. J. Lomas, K. Lawson, H. W. Morsi, P. Nielsen, D. F. H. Start, A. Tanga, A. Taroni, K. Thomsen and D. J. Ward, Nucl. Fusion **33** 1319 (1993).

[5] S. D. Scott, M. C. Zarnstorff, C. W. Barnes, R. Bell, N. L. Bretz, C. Bush, Z. Chang, D. Ernst, R. J. Fonck, L. Johnson, E. Mazzucato, R. Nazakian, S. Paul, J. Shivell, E. J. Snyakowski, H. Adler, M. Bell, R. Budny, R. Fredrickson, B. Grek, A. Janos, D. Johnson, D. McCune, H. Park, A. Ramsey, M. H. Redi, G. Taylor, M. Thompson, and R. Weiland, Phys. Plasmas **2** 2299 (1995).

[6] C. W. Barnes, S. D. Scott, M. G. Bell, R. Bell, R. V. Budny, C. E. Bush, E. D. Fredrickson, B. Grek, K. W. Hill, A. Janos, J. H. Kamperschroer, P. H. LaMarche, D. K. Mansfield, H. K. Park, C. K. Phillips, A. T. Ramsey, J. Schivell, B. C. Stratton, E. J. Synakowski, G. Taylor, J. R. Wilson, and M. C. Zarnstorff, Phys. Plasmas **3** 4521 (1996).

[7] J. Jacquinot and JET Team Nucl. Fusion **38** 1263 (1999).

[8] J. G. Cordey, B. Balet, D. V. Bartlett, R. V. Budny, J. P. Christiansen, G. D. Conway, L.-G. Eriksson, G. M. Fishpool, C. W. Gowers, J. C. M. de Haasb, P. J. Harbour, L. D. Horton, A. C. Howman, J. Jacquinot, W. Kerner, C. G. Lowry, R. D. Monk, P. Nielsen, E. Righi, F. G. Rimini, G. Saibene, R. Sartori, B. Schunke, A. C. C. Sips, R. J. Smith, M. F. Stamp, D. F. H. Startc, K. Thomsen, B. J. D. Tubbing and M. G. von Hellermann, Nucl. Fusion **39** 301 (1999).

[9] H. Urano, T. Takizuka, Y. Kamada, N. Oyama, H. Takenaga and the JT-60 Team, Nucl. Fusion **48** 045008 (2008).

[10] H. Urano, T. Takizuka, M. Kikuchi, T. Nakano, N. Hayashi, N. Oyama, and Y. Kamada, Phys. Rev. Lett. **109** 125001 (2012).

[11] H. Urano, T. Takizuka, N. Aiba, M. Kikuchi, T. Nakano, T. Fujita, N. Oyama, Y. Kamada, N. Hayashi and the JT-60 Team, Nucl. Fusion **53** 083003 (2013).

[12] A. D. Gurchenko, E. Z. Gusakov, P. Niskala, A. B. Altukhov, L. A. Esipov, T. P. Kiviniemi, T. Korpilo, D. V. Kouprienko, S. I. Lashkul, S. Leerink, A. A. Perevalov and M. A. Irzak, Plasma Phys. Control. Fusion **58** 044002 (2016).

[13] P. A. Schneider, A. Bustos, P. Hennequin, F. Ryter, M. Bernert, M. Cavedon, M. G. Dunne, R. Fischer, T. Görler, T. Happel, V. Igochine, B. Kurzan, A. Lebschy, R. M. McDermott,

P. Morel, M. Willensdorfer, the ASDEX Upgrade Team and The EUROfusion MST1 Team, Nucl. Fusion **57** 066003 (2017).

[14] F. M. Laggner, E. Wolfrum, M. Cavedon, F. Mink, M. Bernert, M. G. Dunne, P. A. Schneider, A. Kappatou, G. Birkenmeier, R. Fischer, M. Willensdorfer, F. Aumayr, EUROfusion MST1 Team, and ASDEX Upgrade Team, Phys. Plasmas **24** 56105 (2017).

[15] P. Niskala, A. D. Gurchenko, E. Z. Gusakov, A. B. Altukhov, L. A. Esipov, M. Yu Kantor, T. P. Kiviniemi, D. Kouprienko, T. Korpilo, S. I. Lashkul, S. Leerink, A.A. Perevalov and R Rochford, Plasma Phys. Control. Fusion **59** 044010 (2017).

[16] C. F. Maggi, H. Weisen, J. C. Hillesheim, A. Chankin, E. Delabie, L. Horvath, F. Auriemma, I. S. Carvalho, G. Corrigan, J. Flanagan, L. Garzotti, D. Keeling, D. King, E. Lerche, R. Lorenzini, M. Maslov, S. Menmuir, S. Saarelma, A. C. C. Sips, E. R. Solano, E. Belonohy, F. J. Casson, C. Challis, C. Giroud, V. Parail, C. Silva, M. Valisa and JET Contributors, Plasma Phys. Control. Fusion **60** 014045 (2018).

[17] I. Pusztai, J. Candy, P. Gohil, Phys. Plasmas **18** 122501 (2011).

[18] A. Bustos, A. Bañón Navarro, T. Görler, F. Jenko, and C. Hidalgo, Phys. Plasmas **22** 012305 (2015).

[19] J. Garcia, T. Görler, F. Jenko and G. Giruzzi, Nucl. Fusion **57**, 014007 (2017).

[20] M. Nakata, M. Nunami and H. Sugama, Phys. Rev. Lett. **118**, 165002 (2017).

[21] C. Estrada–Mila, J. Candy and R. E. Waltz, Phys. Plasmas **12**, 022305 (2005).

[22] A. G. Peeters, Y. Camenen, F. J. Casson, W. A. Hornsby, A. P. Snodin, D. Strintzi. and G. Szepesi, Comp. Phys. Comm. **180**, 2650 (2009).

[23] E. Fable, C. Angioni and O. Sauter, Plasma Phys. Control. Fusion **52** 015007 (2010).

[24] C. Angioni, J. Candy, E. Fable, M. Maslov, A. G. Peeters, R. E. Waltz, and H. Weisen, Phys. Plasmas **16** 0607702 (2009).

[25] C. Angioni, E. Fable, M. Greenwald, M. Maslov, A. G. Peeters, H. Takenaga and H. Weisen, Plasma Phys. Control. Fusion **51** 124017 (2009).

[26] C. Angioni, Y. Camenen, F. J. Casson, E. Fable, R. M. McDermott, A. G. Peeters and J. E. Rice, Nucl. Fusion **52** 114003 (2012).

[27] T. Hein, C. Angioni, E. Fable and J. Candy, Phys. Plasmas **17**, 102309 (2010).

[28] T. Casper, Y. Gribov, A. Kavin, V. Lukash, R. Khayrutdinov, H. Fujieda, C. Kessel for the ITER Organization and ITER Domestic Agencies, Nucl. Fusion **54**, 013005 (2014).

[29] R. L. Miller, M. S. Chu, J. M. Greene, Y. R. Lin-Liu, R. E. Waltz, Phys. Plasmas **5**, 973 (1998).

[30] H. Weisen, A. Zabolotsky, C. Angioni, I. Furno, X. Garbet, C. Giroud, H. Leggate, P. Mantica, D. Mazon, J. Weiland, L. Zabeo, K.-D. Zastrow and JET-EFDA contributors, Nucl. Fusion **45**, L1 (2005).

[31] C. Angioni, A. G. Peeters, F. Ryter, F. Jenko, G. D. Conway, T. Dannert, H.U. Fahrbach, M. Reich, W. Suttrop, the ASDEX Upgrade Team, L. Fattorini, Phys. Plasmas **12**, 040701 (2005).

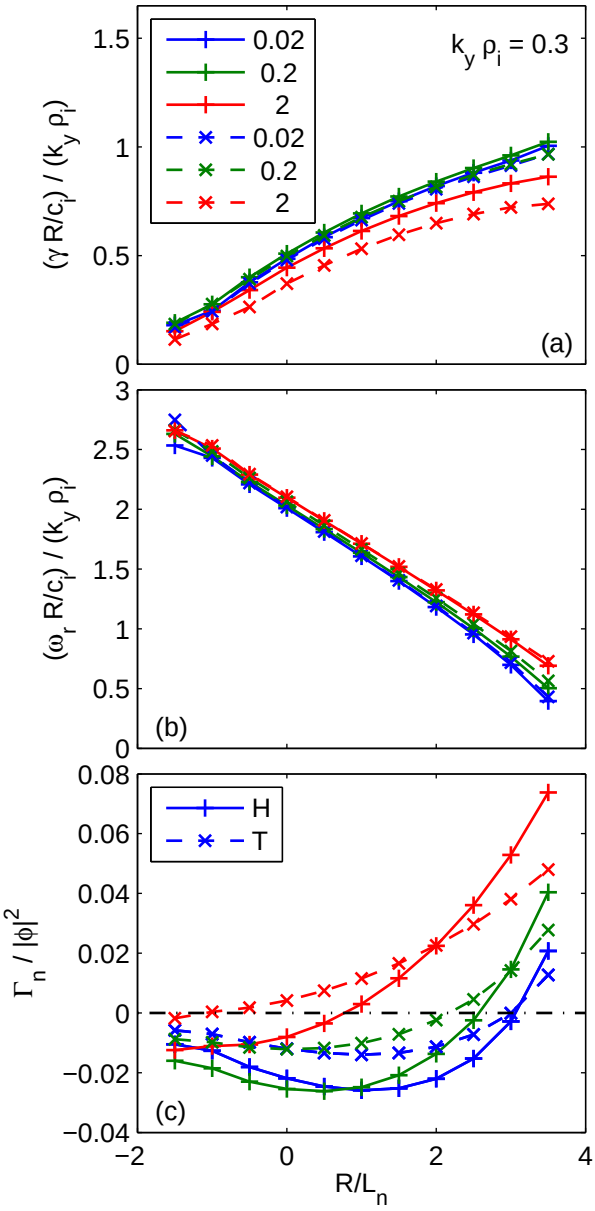


FIG. 2: Dependence of the normalized growth rate (a), real frequency (b) and quasi–linear particle flux as a function of the normalized logarithmic density gradient $R/L_n$ for H and T at different values of collisionality at a fixed binormal wave number $k_y\rho_i = 0.3$, normalized to the Larmor radius of the main ion species. In the legend (a) the corresponsing values of collisionality, provided by the product $Rn_e/T_e^2$, are reported, with $R$ in meters, $n_e$ in $10^{19}$ m$^{-3}$ and $T_e$ in keV.

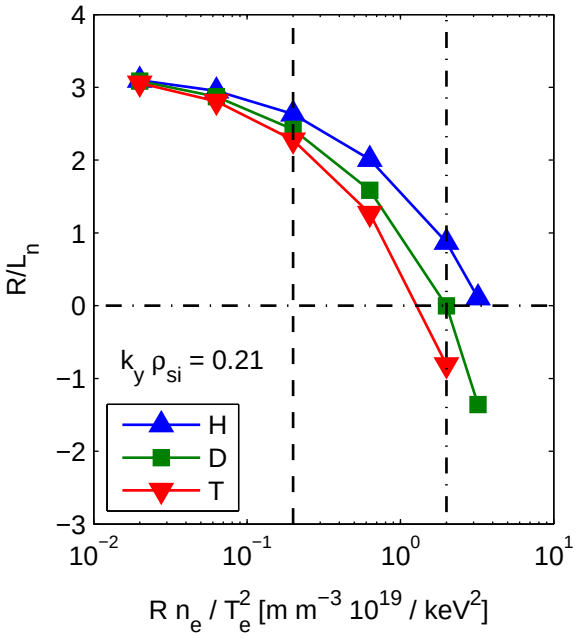


FIG. 3: Values of the normalized logarithmic density gradient $R/L_n$ for H, D and T at the null of the quasi–linear particle flux as a function of collisionality at a fixed representative binormal wave number $k_y\rho_i = 0.3$, normalized to the Larmor radius of the main ion species. In the x-axis the the collisionality is directly provided by the product $Rn_e/T_e^2$, with $R$ in meters, $n_e$ in $10^{19}$ m$^{-3}$ and $T_e$ in keV. Vertical lines identify collisionality values of a low collisionality (low density, high power) plasma in present devices (dashed), which is practically equal to the collisionality of a burning plasma at high density in a reactor, and the indermediate to high collisionality range of a plasma (at high density, and moderate power) in present devices (dash–dotted).

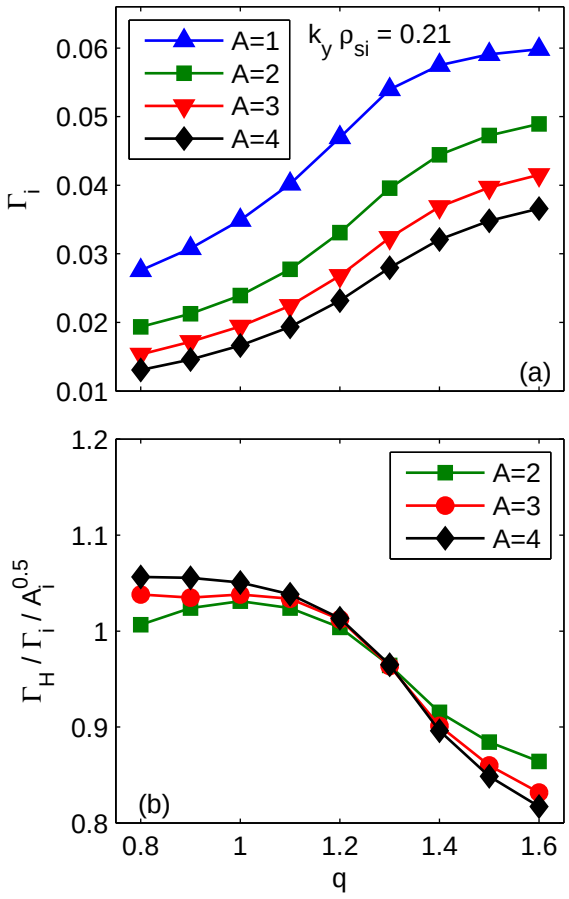


FIG. 4: Dependence of the electron particle flux as a function of the safety factor at $r/R = 10^{-4}$, with $R/L_{Ti} = 9$, $R/L_{Te} = 0$ and $R/L_n = 0$ (a). The ratios of the particle fluxes are almost exactly proportional to $(m_e/m_i)^{0.5}$ in the limit of small safety factor (b).

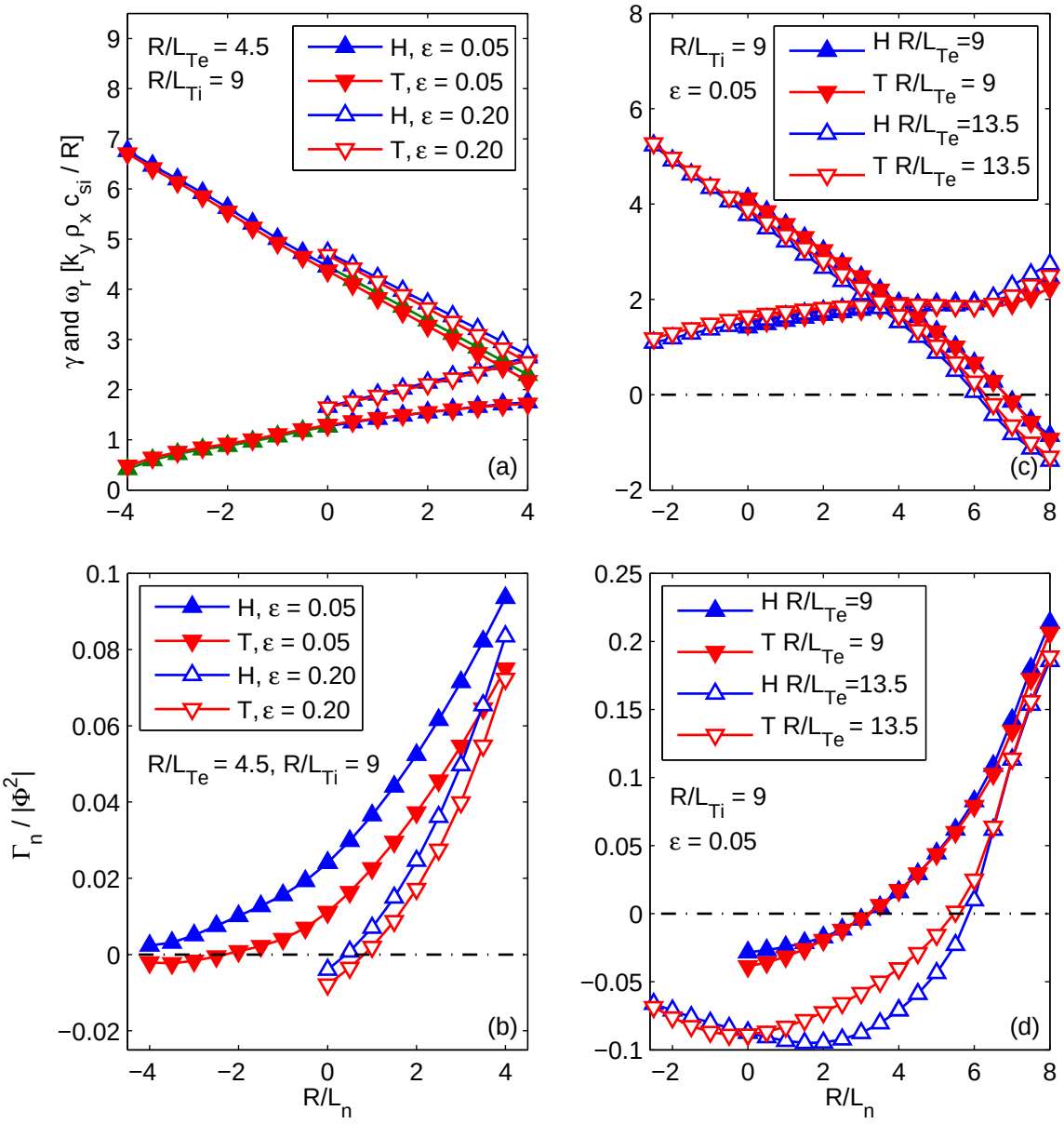


FIG. 5: Linear growth rates and more frequencies (a,c) and corresponding quasi–linear particle fluxes, normalized to the electrostatic potential amplitude sqaured, as a function of $R/L_n$ with H and T as ion species and for different choices of input parameters: $R/L_{Te} = 4.5$ and $R/L_{Ti} = 9$ with $\epsilon = 0.05$ and $\epsilon = 0.20$ in (a,b), as well as $R/L_{Te} = 9.0$ and $R/L_{Te} = 13.5$ with $R/L_{Ti} = 9.0$ and $\epsilon = 0.05$ in (c,d). Combinations of passing and trapped contributions produce different dependences (collisionless limit).

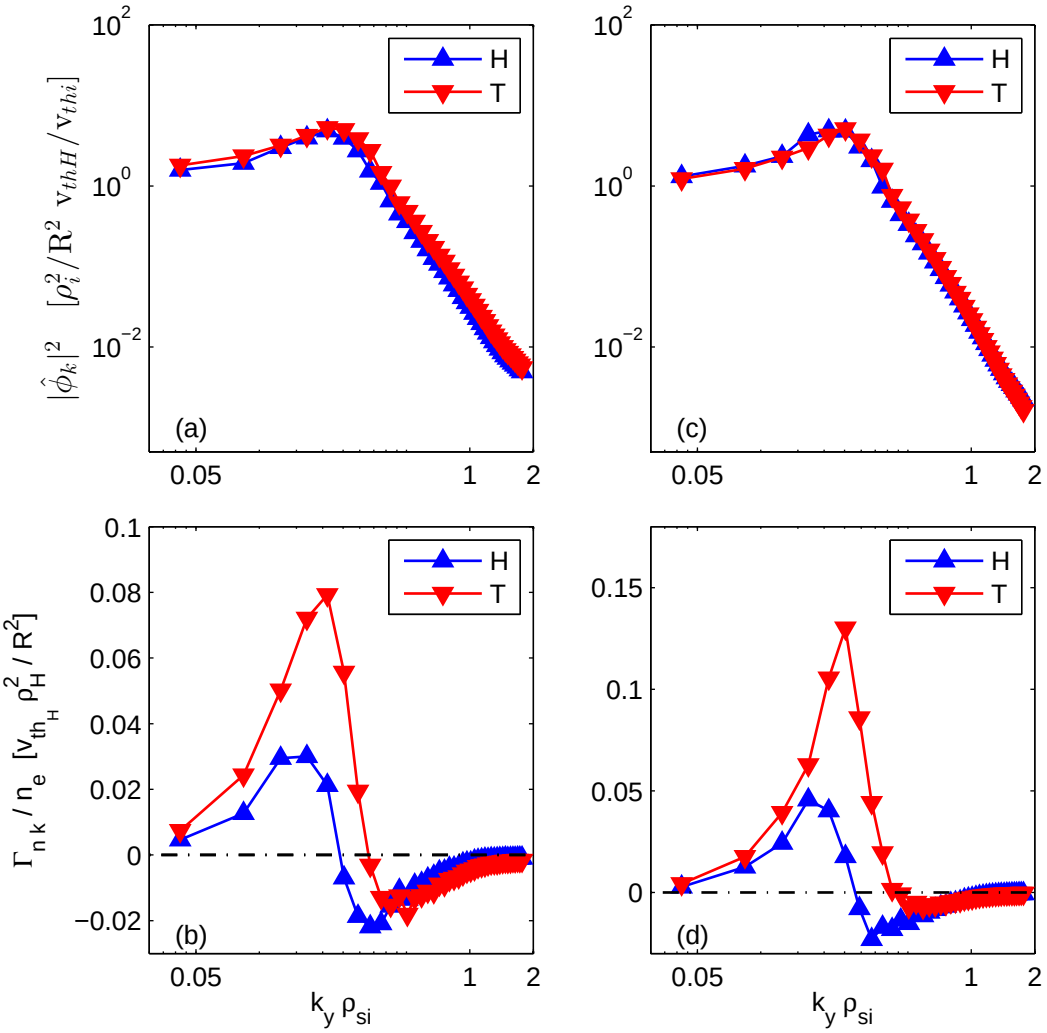


FIG. 6: Nonlinear binormal wave number spectra of the squared electrostatic potential fluctuations (a,c) and of the particle flux (b,d), for simulations with main ion H (triangles pointing up) and T (triangles pointing down) at two different collisionalities, with $\overline{\nu} = 0.2$ and $R/L_n = 2.5$ (a,b) and with $\overline{\nu} = 2$ and $R/L_n = 1.5$ (c,d). The squared electrostatic potential fluctuations (a,c) have been normalized to $(\rho_i/R)^2 v_{thH}/v_{th_i}$, implying that identical spectra moving from H to T would satisfy the condition of exact gyro–Bohm scaling of the fluxes. The particle flux spectra have been normalized to the the same gyro–Bohm factor computed with the H mass, namely $v_{thH}(\rho_H/R)^2$.

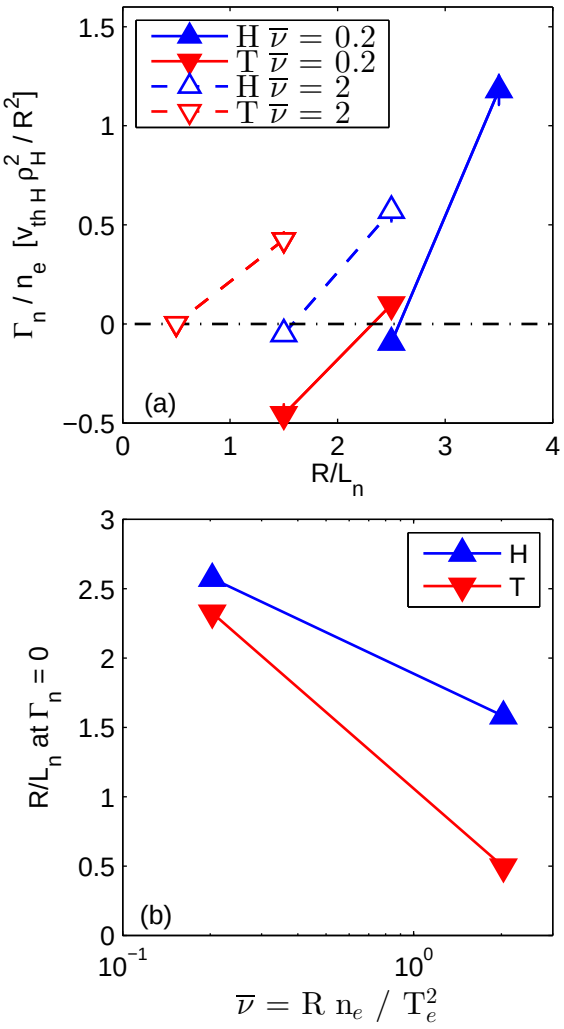


FIG. 7: Nonlinear particle fluxes as a function of $R/L_n$ with H and T as main ion mass at different collisionality parameter $\overline{\nu} = Rn_e/T_e^2$ (a) and corresponding values of $R/L_n$ fulfilling the condition of $\Gamma = 0$ as a function of the same collisionality parameter $\overline{\nu}$.

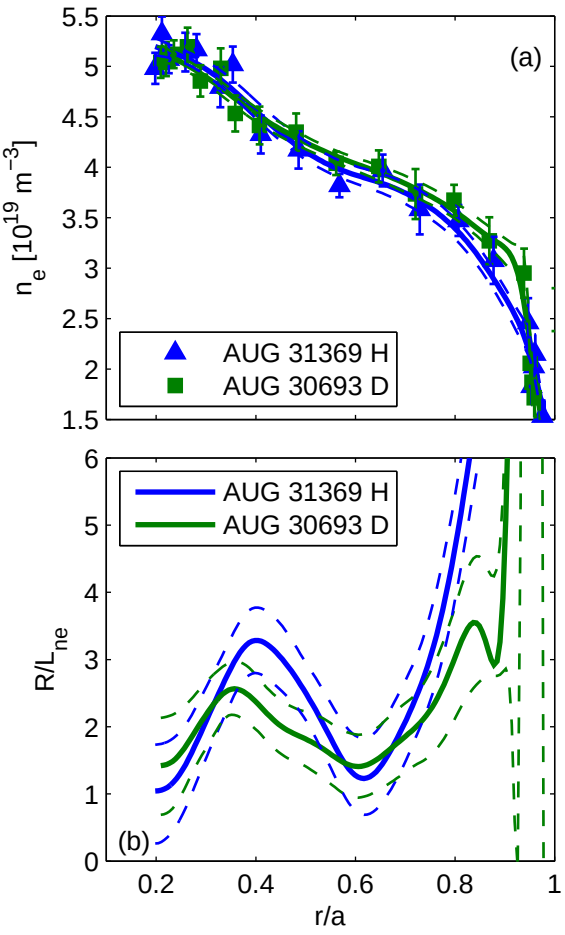


FIG. 8: Comparison of electron density profiles (a) and related normalized logarithmic density gradients (b) for a pair of AUG plasmas in H (triangles) and in D (squares) where heating powers have been adjusted in order to obtain the best match of the electron and ion temperature profiles [13].

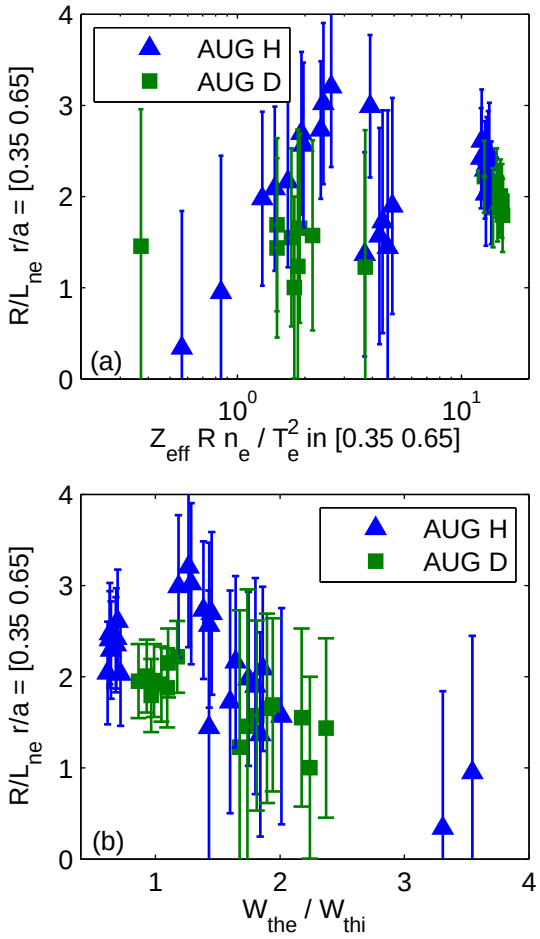


FIG. 9: Radial average of the normalized logarithmic electron density gradient around mid–radius as a function of the collisionality parameter $Z_{\rm eff} R n_e / T_e^2$ [$R$ in m, $n_e$ in m$^{-3}$ and $T_e$ in keV] (a) and as a function of the electron to ion total stored energy from an AUG dataset of H (triangles) and D (squares) plasmas without NBI heating.

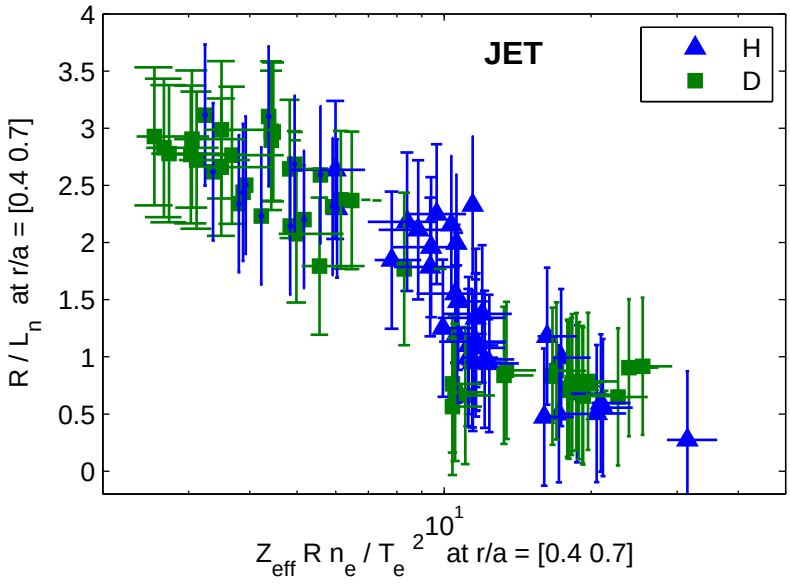


FIG. 10: Scatter plot of the normalized logarithmic density gradient of the electron density as a function of the collisionality factor $Z_{\rm eff} n_e R/T_e^2$, with $n_e$ in $10^{19}$ m$^{-3}$, $R$ in m and $T_e$ in keV, for JET plasmas in H (triangles) and in D (squares), measured by the HRTS system. Both quantities have been averaged over a radial domain around mid–radius. Plasmas with at the most one positive ion neutral injector (PINI) of the JET NBI system have been considered.